

## Identification of amorphous phases in the Fe–Ni–Co ternary alloy system using continuous phase diagram material chips

Young K. Yoo<sup>a</sup>, Qizhen Xue<sup>a</sup>, Yong S. Chu<sup>b</sup>, Shifa Xu<sup>c</sup>, Ude Hangen<sup>d</sup>, Hyung-Chul Lee<sup>a</sup>,  
Wolfgang Stein<sup>d</sup>, Xiao-Dong Xiang<sup>a,\*</sup>

<sup>a</sup>Intematix Corporation, 351 Rheem Blvd, Moraga, CA 94556, USA

<sup>b</sup>Advanced Photon Source, Argonne National Lab, Argonne, IL 60439, USA

<sup>c</sup>SRI International, 333 Ravenswood Ave, Menlo Park, CA 94025-3493, USA

<sup>d</sup>SURFACE, nanoLab, Rheinstrasse 7, 41836 Hueckelhoven, Germany

Received 1 January 2005; accepted 31 May 2005

Available online 30 August 2005

### Abstract

In conventional bulk alloy phase diagrams, each discrete composition point is prepared and characterized one at a time, and consequently has a different thermodynamic history. The continuous phase diagram (CPD) offers a unique opportunity to conduct high throughput construction of thin film phase diagram with single universal thermodynamic history applied to all the compositions. Here, we performed the CPD experiment of Fe–Ni–Co ternary alloy system using combinatorial ion beam sputtering system. The high throughput screenings of structural and physical properties were made using scanning microbeam X-ray diffractometer, scanning magneto-optic Kerr effect (SMOKE) measurement, and scanning nano-indentation microscope. The results are consistent with the known structural phases and phase boundaries. In addition, we identified two very narrow amorphous regions, carefully examined and confirmed by synchrotron microbeam X-ray diffraction studies.

© 2005 Published by Elsevier Ltd.

**Keywords:** A. Ternary alloy systems; B. Glasses, metallic; B. Phase diagrams; C. Thin films

Since 1960 s, materials scientists and condensed matter physicists have made efforts to develop more effective methods to construct phase diagrams. The ‘composition spread’ technique represents an approach that utilizes natural gradient profiles generated by off-axis sputtering or other physical deposition process [1–6]. Usually, the off-axis co-sputtering of multiple targets generates an 1-dimensional or 2-dimensional non-linear map of varied composition, which is then transformed into a standard linear representation of phase diagram with the help of composition analysis techniques. Another approach uses diffusion couples, triples, and higher order multiples to map the structural phase diagram [7,8]. In this technique, a naturally occurring diffusion region of tens of microns is

utilized to map the structural and physical property phase diagrams with the help of high resolution composition, structure and physical property analysis tools. This technique is especially useful for structural materials studies; however, it presents relatively high barriers in both cost and technical feasibility to researchers.

In recent years, we have developed a continuous phase diagram (CPD) mapping technique, where the composition is continuously varied as a direct image of the traditional linear representation of phase diagram, i.e. equilateral triangle for a ternary phase diagram. This technique eliminates the requirement of composition analysis and transformation of nonlinear profiles into the standard linear profiles of composition and corresponding physical properties. It has been used in the comprehensive mapping of 1- and 2-D physical property phase diagrams of complex materials systems [9–11] and 1-D structural and physical property phase diagrams [12].

We present here a detailed phase diagram mapping of crystal structure and physical properties of the well-studied  $\text{Fe}_{1-x-y}\text{Ni}_x\text{Co}_y$  ternary alloy system. Soft magnetic

\* Corresponding author. Tel.: +1 925 631 9005x112; fax: +1 925 631 7892.

E-mail address: [xdxiang@intematix.com](mailto:xdxiang@intematix.com) (X.-D. Xiang).

materials and many industrially significant alloys, such as permalloy, are contained in the system. Moreover, various nano-phases including amorphous phases have been explored in order to tailor their magnetic and mechanical properties [13,14]. The constructed phase diagrams from CPD mapping are consistent with known structural phases from existing literature and database. More importantly, two amorphous phase regions were identified and confirmed by synchrotron microbeam X-ray diffraction studies. The present amorphous phases, which require neither rapid solidification nor heavy element doping, are clearly composition dependent, and raise an important possibility of the current approach in nanomaterials research and their applications.

The thin film metal alloy ternary phase diagram was fabricated on a sapphire (0001) substrate of a 1.16 cm (B) × 1 cm (H) equilateral triangle shape with Fe/Ni/Co multi-layered films deposited, about 1000 Å thick, at room temperature using a combinatorial ion-beam-sputtering deposition system, similarly to that of previous work on  $\text{Fe}_{1-x}\text{Ni}_x$  CPD [12]. As-grown multi-layered films were annealed in the vacuum chamber at 600 °C and  $10^{-8}$  Torr for 3 h to obtain full compositional mixing normal to the film plane without oxidation and to achieve alloy phase formation. The sample was quenched at the rate of 5 °C/min in vacuum after annealing.

After the Fe–Ni–Co ternary CPD sample is fabricated, X-ray diffraction (XRD) study using a laboratory source indicated highly oriented growth of the film. A detailed structural characterization was made by scanning microbeam X-ray diffractometer, manufactured by Intematix, with spatial resolution in the range of 50–300 µm. This instrument with 5 kW Cu tube can also perform simultaneous X-ray fluorescence to confirm the composition profile of a sample. It utilizes a unique high brilliance X-ray microfocus source with capillary waveguide. The focused flux intensity is at least 10–20 times higher than pinhole configuration with the same X-ray source. Three hundred micrometers XRD beam spot was used and over 1000 composition points were scanned and measured for this continuous phase diagram chip.

Using the scanning microbeam X-ray diffractometer, a  $2\theta$  range of  $4^\circ$  was scanned, which is sufficient to cover the angular range of the characteristic diffraction peaks of Fe, Ni, Co, and other well-known compound phases. For each ( $\theta-2\theta$ ) diffraction peak profile at a given composition point, three attributes: peak intensity, the  $2\theta$  position of peak center, and full-width half-maximum (FWHM) were obtained by fitting the peak profile with a Lorentian curve. From the  $2\theta$  position of the center of each peak, we determined the crystalline phases and structures. Fig. 1 shows three selected scans of XRD along Ni–Fe, Fe–Co, and Co–Ni edge, basically binary alloy systems of this ternary CPD sample, respectively. Note that all three known structural phases in this system are identified in the XRD maps of each binary alloy system. Ni FCC and Fe BCC

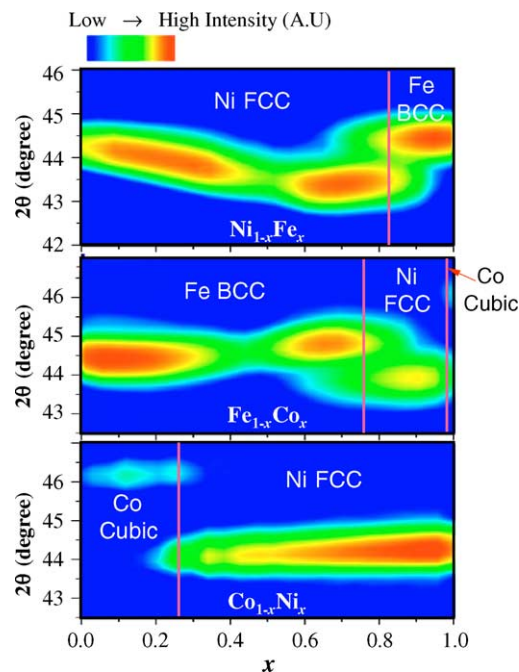


Fig. 1. Linear scans of XRD along Ni–Fe, Fe–Co, and Co–Ni edge of Fe–Ni–Co ternary CPD sample by Intematix's scanning microbeam XRD. Three structural phases are denoted. The scan along each edge consists of a binary alloy system of (a)  $\text{Ni}_{1-x}\text{Fe}_x$ , (b)  $\text{Fe}_{1-x}\text{Co}_x$ , (c)  $\text{Co}_{1-x}\text{Ni}_x$ .

denote Ni–Fe alloys with FCC and BCC structures. In other words, there is no phase separation.

The details of structural changes and progression are clearly demonstrated in Fig. 1. Since the beam spot size was 300 µm diameter, while the compositional resolution was below 50 µm and the measurements were made to result in sufficient intensities, the XRD scan along each binary system contains a small fraction of the third element. For example, Fig. 1a may represent Fe–Ni binary system with small fraction of Co. Still, Fig. 1a closely follows the result from previous work in  $\text{Fe}_{1-x}\text{Ni}_x$  CPD experiment using synchrotron microbeam X-ray source [12]. The red lines in each binary system of Fig. 1 mark the phase transition boundaries. Note that across each phase boundary the intensity of one phase decreases while that of the other phase increases. However, the intensity decrease within the FCC phase of Fig. 1a and BCC phase of Fig. 1b does not correspond to a 1st order transition of structural phases, which will be discussed later.

Fig. 2 shows the colored maps of the three attributes of each structural phase. There are a few distinct features of phase boundaries in these plots. For a given structural phase, the peak intensity allows us to map the extent of each phase in compositional space. There is a clear overlap between the phases, i.e. the compositions at which both phases co-exist. We also observe widening FWHM near the phase boundary. The detailed change in  $2\theta$  peak position is also probed in these plots. The entire ternary phase diagram was constructed by merging the three peak intensity plots of

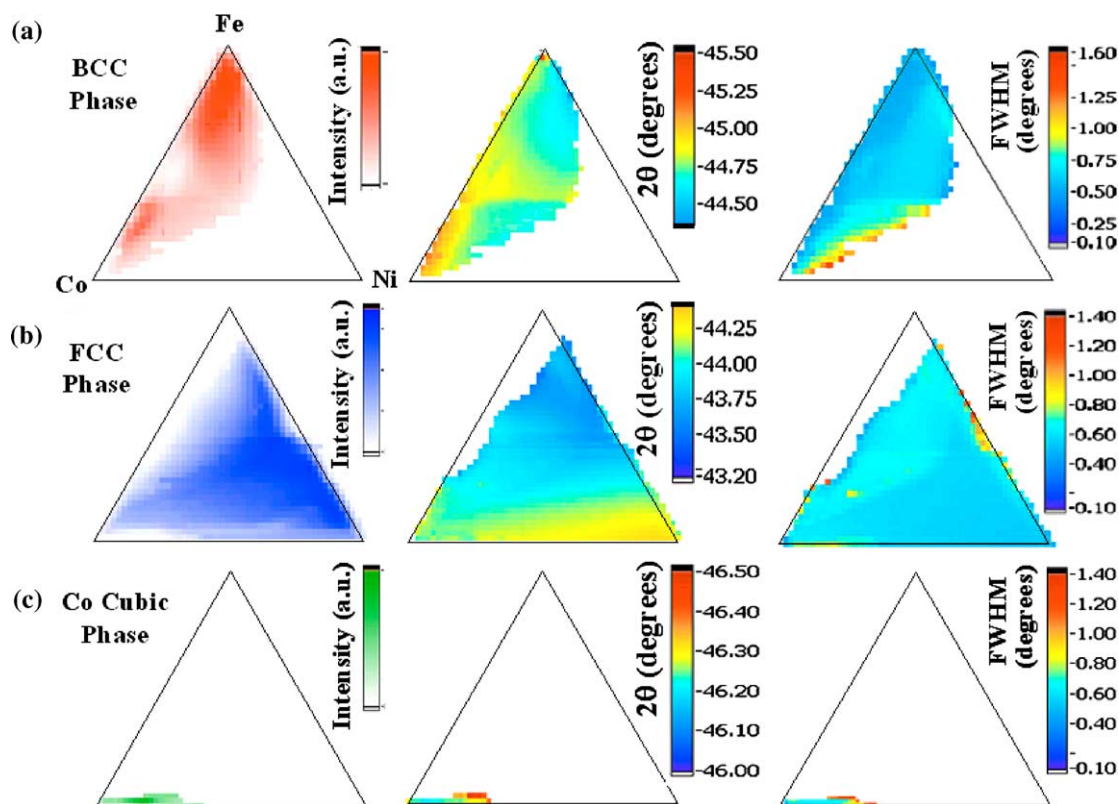


Fig. 2. XRD peak intensity,  $2\theta$  position, and FWHM of (a) FCC, (b) BCC, and (c) Co Cubic phase in the Fe–Ni–Co ternary CPD sample by Intematix's scanning microbeam XRD.

the three phases as shown in Fig. 3a. The result is consistent with all the known structural phases in this alloy system, and closely follows the previously reported phase diagrams constructed by a series of discrete data points obtained with individual samples. The overlap (co-existence) of two structural phases is the distinctive feature of the constructed phase diagram, and indicates the non-equilibrium thermodynamic nature of the sample, where a kinetic barrier of phase growth impedes the sample from forming a single phase. In most bulk alloy phase diagrams, each composition point is processed under different thermodynamic conditions, generally quenched at different rates, to force a single phase. The current CPD sample in thin film represents a unique phase diagram of this alloy system with a single universal thermodynamic history applied to all the compositions.

The magnetic property of the CPD sample was investigated by the SMOKE system (Fig. 3b). A qualitative saturation magnetic moment of each point of the ternary phase diagram was mapped through the difference in magneto-optical Kerr rotations at  $\pm 50$  Oe applied magnetic field (a higher field gives rise to similar mapping) parallel to the thin film plane. Since the entire hysteresis curve at each point can be measured, other properties, such as coercivity, can also be extracted, whose detail will be published elsewhere. We observed that Kerr rotations are also

contrasted along the phase boundaries defined from the structural phase diagram.

The mechanical properties of thin films can be tested by nano-indentation experiments. A calibrated diamond indenter with Berkovich geometry, 3-sided-pyramid with opening angle of  $142.3^\circ$  between edge and opposite plane, (the inset of Fig. 3c) was used to perform a grid of 300 indents across the sample. A drift check was performed prior to the indentation tests. The resulting load–displacement–curves were analysed by the method described by Oliver and Pharr [15]. The hardness is calculated with

$$H = \frac{P_{\max}}{A(h_c)} \quad (1)$$

where  $P_{\max}$  is the maximum load,  $A(h_c)$  is a calibrated area function found by indentation experiments on a standard sample, and  $h_c$  is the contact depth.

The CPD sample shows a clear trend in the Hardness (GPa) map along the phase boundaries identified from structural mapping (Fig. 3c). The region of the sample that had been identified to be of FCC symmetry is soft and the region containing FCC and BCC or pure BCC crystal structure is hard. This effect is due to the differences in Peierls Stress necessary to move dislocations [15]. The dislocation movement that acts as major deformation mechanism in metals is easier in FCC than in BCC metals.

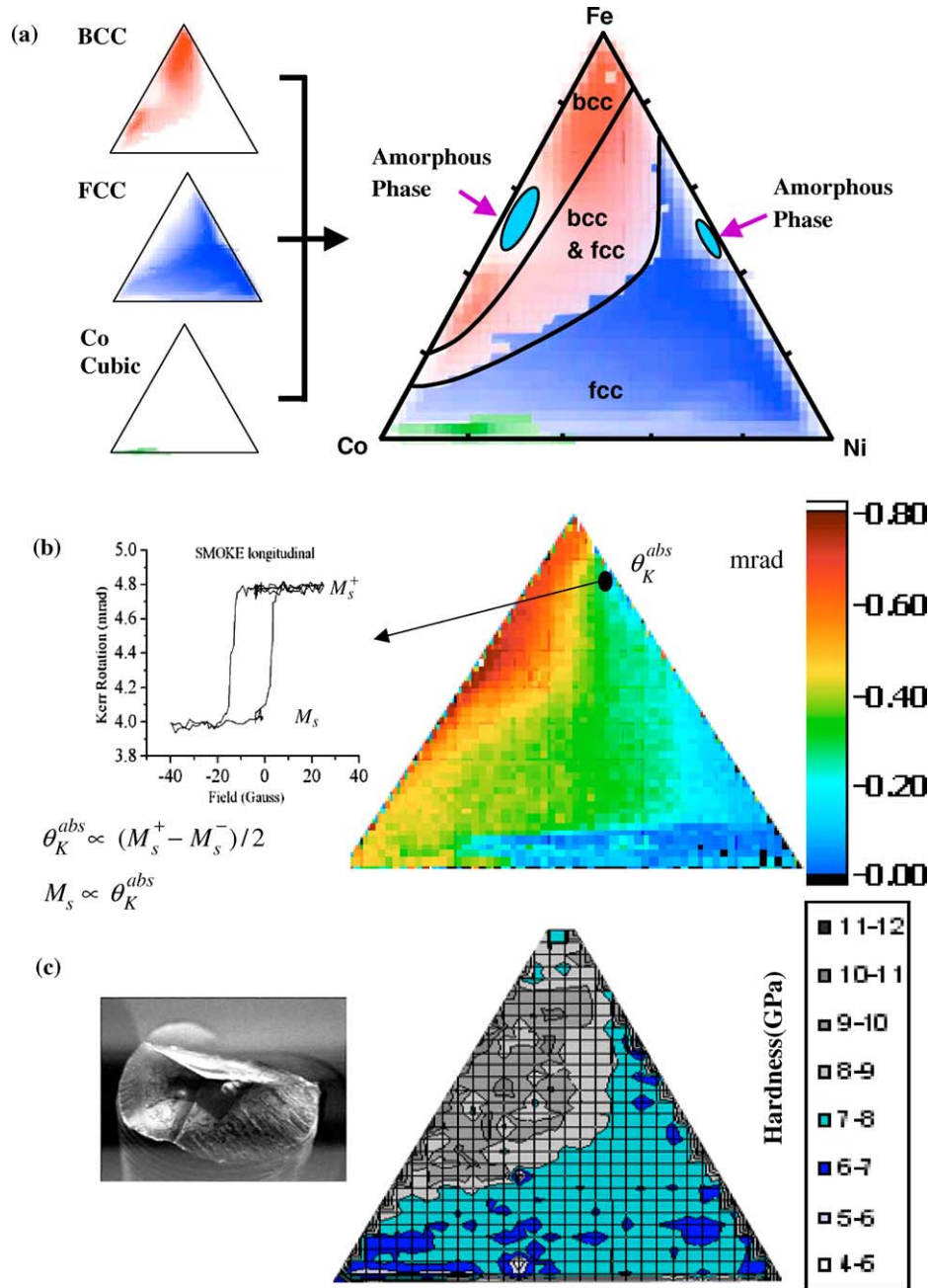


Fig. 3. Rapid construction of Fe–Ni–Co ternary phase diagrams of (a) structural property by converging three XRD peak intensity plots of FCC, BCC, and Co Cubic phases, (b) magnetic property by SMOKE, where the difference in magneto-optical Kerr rotations is measured at  $\pm 50$  Oe applied magnetic field, and (c) mechanical property through hardness measurement by scanning nano-indentation. The inset shows Berkovich Diamond Indenter, 3-sided-pyramid, with opening angle of  $142.3^\circ$  between edge and opposite plane.

For this reason the FCC region is much softer. For single bulk samples, the hardness depends on the history of the sample (solidification, annealing, deformation and other treatments) and thus, their mechanical properties cannot be compared directly unless one successfully manages to fabricate bulk samples under identical thermodynamic conditions and history. In the current CPD sample, the same history of synthesis and annealing treatments is

uniformly applied and thus the mechanical differences are much more pronounced.

The most striking feature of this continuous phase diagram is two regions, designated as ‘amorphous phase’ in Fig. 3a, where the peak intensity suddenly drops to near noise level as shown in Figs. 4 and 5. X-ray fluorescence confirmed that the elemental composition across these regions vary linearly in the same way as in



the rest of the sample. Thus, this sudden decrease in the diffraction intensity cannot be explained in term of the film-thickness, due to any possible anomaly in the deposition. In addition, the significantly reduced intensity in these regions was reproduced in CPD samples, fabricated under the same annealing condition. In order to further investigate these regions of low diffraction intensity with higher spatial resolution and counting statistics, we have carried out synchrotron measurement using the scanning microdiffraction set-up at 2-BM of the Advanced Photon Source (APS). A 12 keV X-ray microbeam with a focal spot size of  $5 \times 5 \mu\text{m}$  was produced using Kirkpatrick–Baez Microfocusing system with 10 cm-long vertical and 20 cm-long horizontal mirrors. The diffraction pattern from the sample was recorded using a CCD ( $2k \times 3k$  pixels with  $18 \text{ mm} \times 27 \text{ mm}$  chip size) position at 45 mm from the sample to have a  $2\theta$  acceptance of  $21^\circ$  with angular resolution of  $0.015^\circ$ . The focusing in the vertical direction gives rise to the instrumental angular resolution (due to convergence angle of the focused beam), which was measured to be  $0.017^\circ$  in full-width half-max. The film exhibited extremely narrow fiber texture, with better than  $0.5^\circ$  in full-width half-maximum of mosaic-spread, along the direction normal to the surface. In order to properly integrate the diffraction intensity, at each measurement

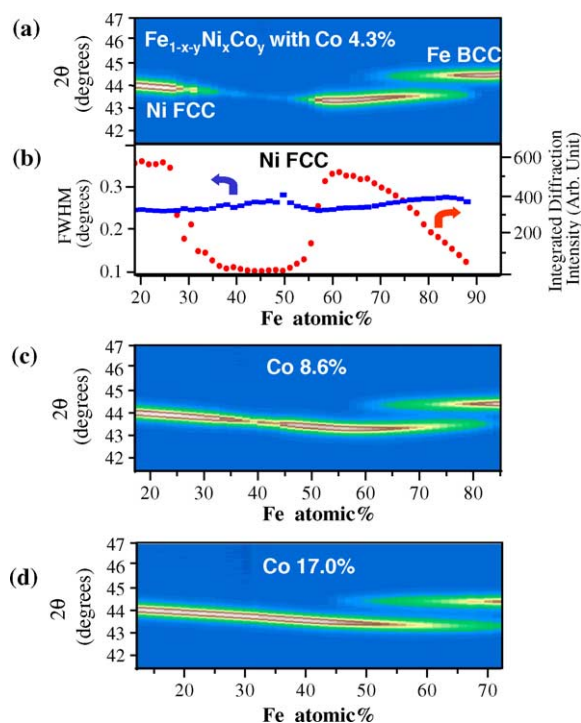


Fig. 4. The integrated diffraction data obtained from the synchrotron microdiffraction measurement on the CPD sample of  $\text{Fe}_{1-x-y}\text{Ni}_x\text{Co}_y$  with Co content fixed (a) at 4.3%, and (b) its FWHM and total integrated diffraction intensity, and with higher Co contents (c) at 8.6%, and (d) at 17%. The  $2\theta$  angles for the integrated diffraction intensity measured at 12 keV were converted to synchronize with the  $2\theta$  angles of laboratory source.

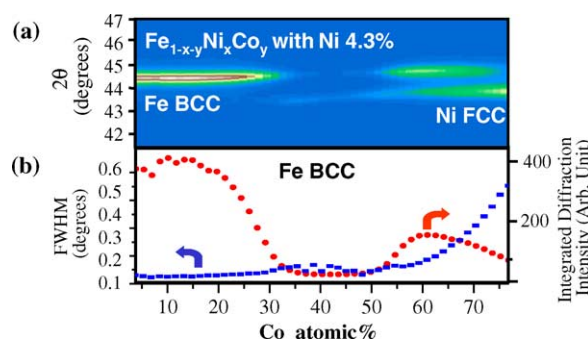


Fig. 5. The integrated diffraction data obtained from the synchrotron microdiffraction measurement on the CPD sample of  $\text{Fe}_{1-x-y}\text{Ni}_x\text{Co}_y$  with Ni content fixed (a) at 4.3% and (b) its FWHM and total integrated diffraction intensity.

point in the CPD sample, the integrated intensity was obtained by rocking the incident beam angle over  $2^\circ$ , which is more than sufficient to integrate over the entire mosaic spread.

Fig. 4a shows the integrated diffraction data obtained from the synchrotron microdiffraction measurement on the CPD sample of  $\text{Fe}_{1-x-y}\text{Ni}_x\text{Co}_y$ , where Fe content changes from 19.2 to 94.7% while Co content is fixed at 4.3%. The  $2\theta$  angles for the integrated diffraction intensity measured at 12 keV were converted so that the comparison between the data obtained using the synchrotron and laboratory source can be easily made. In Fig. 4a, we first observe the distinct presence of Fe BCC and Ni FCC phases with the phase transition occurring at  $x = 0.83$ . Between Fe content of 71 and 89%, there is the overlap (co-existence) of BCC and FCC phases. The most important feature of Fig. 4a is the dramatic decrease in synchrotron XRD intensity for the composition range of  $0.35 < \text{Fe content} < 0.53$ . Higher spatial resolution ( $5 \mu\text{m}$ ) and angular resolution ( $0.01^\circ$ ) provides much higher sensitivity to the change in the diffraction intensity. Fig. 4b plots the full-width half-maximum (FWHM) and total integrated diffraction intensity. In particular, the total integrated intensity at 43% Fe content is about 40 times weaker than the diffraction intensity at 25% Fe. For this composition region, there is no other diffraction intensity corresponding to other crystalline phases either due to impurity or phase separation, over  $40^\circ$  in  $2\theta$  angular ranges, the angular acceptance of the CCD. In addition, we have not observed any significant change in mosaic spread in this region. Also, we could not observe any optical difference in terms of surface quality over the sample, which has mirror-like surface smoothness. In Fig. 4b, the full-width half-maximum (FWHM) of the diffraction peaks in Fig. 4a, which exhibits small increase ( $\sim 10\%$ ) in the peaks width, which might be interpreted peak broadening due to the decrease in average crystalline size. However, this effect is not so dramatic in comparison with the other composition region of the sample. The instrumental resolution due to the CCD pixel size and

the vertical convergence angle of the incident beam is negligible to the measured peak width.

Considering all these findings, we conclude that the dramatic loss in the diffraction intensity results from the formation of amorphous alloys in this composition range. The composition range of the amorphous region depends on the Co concentration. Fig. 4c and d show the progression of this amorphous phase region with increasing Co contents of 8.6 and 17%. With increasing Co content, the amorphous phases disappear quickly. We also identify the amorphous phase region at different part of the ternary phase diagram. Fig. 5 shows the integrated diffraction intensity map, FWHM, and total diffraction intensity of the CPD sample of  $\text{Fe}_{1-x-y}\text{Ni}_x\text{Co}_y$ , where Co content changes from 3.4 to 76.4% while Ni content is fixed at 4.3%. Here, we observe a small trace of FCC phase extended into the amorphous phase region with most of diffraction intensity of FCC phase lost. More dramatically, the integrated diffraction intensity of BCC phase is completely lost near 41% of Co. In this region, the peak width has been broadened more than that of the Ni FCC structure. However, it is still negligible compared with the peak broadening at the coexistent region between FCC and BCC.

Very small increase in the diffraction peak width in both amorphous regions can be interpreted as small reduction in the average particle size of the crystalline grains. However, this broadening is dwarfed by the clear and steady increase in peak width across co-existing FCC–BCC region. We have not observed significant change in fiber texture throughout this region in terms of significant change in the mosaicity or increase intensity for Debye–Scherrer ring. We also have not observed the additional diffraction pattern over  $\sim 21^\circ$  angular range  $2\theta$  of the CCD detector. In these amorphous regions, the significant loss of the integrated diffraction intensity strongly points to the amorphous phase formation since most of diffraction intensity is lost [16]. If the phases had been nanocrystalline, FWHM should increase significantly; and moreover, the intensity integrated over  $2\theta$  and rocking curve angle should not change. Unfortunately, we have not observed the increase in the diffuse scattering at the angular position corresponding to inter-atomic distance of Fe–Ni or Fe–Co, which is one of the characteristic signatures of the amorphous phase. The lack of the observation of the diffuse scattering is most likely due to the lack of the dynamic range of the CCD used for the measurement and insufficient dwelling time for the data collection. Measurement of weak intensity is challenging with a CCD detector because of the thermal noise, which increases with the acquisition time.

Most of alloy materials can be prepared in amorphous phases under special processing conditions such as rapid solidification or heavy metal ion implantation [14,17]. The present system consists of three highly soluble transition metals without any addition of heavy metals such as rare earth or non-metallic elements such as B, Si, etc.

Furthermore, occurrence of these two amorphous phases does not seem to be related to the cooling rate in the annealing process since at least two significantly different cooling rates of 0.5 and  $5^\circ/\text{min}$  made no difference. At this point, the mechanism of these amorphous magnetic phases in the thin film of this classically well-known metallurgical system is not clear. Current method may also be useful in searching for metallic glasses, which often possess significantly improved mechanical properties, wear and corrosion resistance, and other desirable physical properties in comparison to their crystalline counterparts [18].

## Acknowledgements

Use of the Advanced Photon Source was supported by the US Department of Energy, Office of Science Basic Energy Sciences, under Contract No. W-31-109-ENG-38.

## References

- [1] Kennedy K, Stefansky T, Davy G, Zackay CF, Parker ER. Rapid method for determining ternary-alloy phase diagrams. *J Appl Phys* 1965;36:3808–10.
- [2] Hanak JJ. Th multiple-sample concept in materials research: synthesis, compositional analysis and testing of entire multicomponent systems. *J Mater Sci* 1970;5:964–71.
- [3] Hanak JJ. Multiple-sample concept: the forerunner of combinatorial materials science. In: Xiang XD, Takeuchi I, editors. *Combinatorial materials synthesis*. New York: Marcel Dekker; 2003. p. 7–34.
- [4] VanDover RB, Schneemeyer LF, Fleming RM. Discovery of a useful thin-film dielectric using a composition-spread approach. *Nature* 1998;392:162–6.
- [5] Van Dover RB, Schneemeyer LF. The continuous composition spread approach. In: Xiang XD, Takeuchi I, editors. *Combinatorial materials synthesis*. New York: Marcel Dekker; 2003. p. 35–68.
- [6] Takeuchi I, Famodu OO, Read JC, Aronova MA, Chang K-S, Craciunescu C, et al. Identification of novel compositions of ferromagnetic shape-memory alloys using composition spreads. *Nat Mater* 2003;2:180–4.
- [7] Hasebe M, Nishizawa T. Application of phase diagrams in metallurgy and ceramics, vol. 2. Washington, DC: NBS special publication 496; 1977. p. 911–54.
- [8] Zhao JC. A combinatorial approach for structural materials. *Adv Eng Mater* 2001;3:143–7.
- [9] Yoo YK, Duewer F, Yang H, Yi D, Xiang X-D. Room temperature electronic phase transitions observed in the continuous phase-diagrams of perovskite manganites. *Nature* 2000;406:704–8.
- [10] Chang H, Takeuchi I. Combinatorial approach to ferroelectric/dielectric materials. In: Xiang XD, Takeuchi I, editors. *Combinatorial materials synthesis*. New York: Marcel Dekker; 2003. p. 69–89.
- [11] Yoo YK, Xiang X-D. Mapping of physical properties: composition phase diagram of complex materials system using continuous composition materials chips. In: Xiang XD, Takeuchi I, editors. *Combinatorial materials synthesis*. New York: Marcel Dekker; 2003. p. 213–62.
- [12] Yoo YK, Ohnishi T, Wang G, Duewer F, Xiang X-D, Chu YS, et al. Continuous mapping of structure–property relations in  $\text{Fe}_{1-x}\text{Ni}_x$ .

- metallic alloys fabricated by combinatorial synthesis. *Intermetallics* 2001;9:541–5.
- [13] Li XG, Takahashi S. Synthesis and magnetic properties of Fe–Co–Ni nanoparticles by hydrogen plasma–metal reaction. *J Magn Magn Mater* 2000;214:195–203.
- [14] McHenry ME, Willard MA, Laughlin DE. Amorphous and nanocrystalline materials for applications as soft magnets. *Prog Mater Sci* 1999;44:291–433.
- [15] Oliver WC, Pharr GM. An improved technique for determining hardness and elastic modulus using load and displacement sensing indentation experiments. *J Mater Res* 1992;7:1564–83.
- [16] McHenry ME, Laughlin DE. Nano-scale materials development for future magnetic applications. *Acta Mater* 2000;48:223–38.
- [17] Luborsky, editor. *Amorphous metallic alloys*. London: Butterworths; 1983.
- [18] Greer AL. Metallic glasses. *Science* 1995;267:1947–53.